






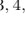









Unprecedented Central Engine “Breathing” Phenomenon in an Active Supermassive Black Hole

SHUYING ZHOU ^{1,2} MOUYUAN SUN ^{1,2} HAI-CHENG FENG ^{3,4,5} SHA-SHA LI ^{3,4,5} YONGQUAN XUE ^{6,7}
JUN-XIAN WANG ^{6,7} ZHEN-YI CAI ^{6,7} JIN-MING BAI ^{3,4,5} DANYANG LI ^{8,1} HENGXIAO GUO ^{9,2} H. T. LIU ^{3,4,5}
KAI-XING LU ^{3,4,5} JIRONG MAO ^{3,4,5} MARCIN MARCULEWICZ ¹ AND JIAN-GUO WANG ^{3,4,5}

¹Department of Astronomy, Xiamen University, Xiamen, Fujian 361005, People’s Republic of China; msun88@xmu.edu.cn

²SHAO-XMU Joint Center for Astrophysics, Xiamen, Fujian 361005, People’s Republic of China

³Yunnan Observatories, Chinese Academy of Sciences, Kunming, Yunnan 650216, People’s Republic of China, hcfeng@ynao.ac.cn, lishasha@ynao.ac.cn

⁴Key Laboratory for the Structure and Evolution of Celestial Objects, Chinese Academy of Sciences, Kunming, Yunnan 650216, People’s Republic of China

⁵Center for Astronomical Mega-Science, Chinese Academy of Sciences, Beijing 100012, People’s Republic of China

⁶Department of Astronomy, University of Science and Technology of China, Hefei, Anhui 230026, People’s Republic of China

⁷School of Astronomy and Space Science, University of Science and Technology of China, Hefei, Anhui 230026, People’s Republic of China

⁸High School Affiliated to Yunnan Normal College, Kunming, Yunnan 650506, People’s Republic of China

⁹Shanghai Astronomical Observatory, Chinese Academy of Sciences, 80 Nandan Road, Shanghai 200030, People’s Republic of China

ABSTRACT

Resolving the inner structures of active galactic nuclei (AGNs) provides the “standard ruler” to measure the parallax distances of the Universe and a powerful way to weigh supermassive black holes (SMBHs). Thanks to time-domain observations, it is possible to use the reverberation mapping (RM) technique to measure time delays between different light curves that probe the structures of the SMBH accretion disks and broad line regions (BLRs), which are otherwise often too compact to be spatially resolved with current facilities for most AGNs. Despite decades of RM studies, the critical physical process that controls the structures of SMBH accretion disk and BLR and their temporal evolution remains unclear. Here we report the variation of the SMBH accretion disk structure of NGC 4151, a highly variable AGN, in response to changes in luminosity within ~ 6 years. In the high-flux state, the time delays measured from our continuum RM with high-cadence (~ 2 days) spectroscopy are $3.8_{-1.0}^{+1.8}$ times larger than that in the low-flux state and 14.9 ± 2.0 times longer than the classical standard thin disk (SSD) prediction. This result provides the first piece of direct evidence that the SMBH disk structure “breathes” in highly-variable AGN manifestations. The significant time-delay change severely challenges the popular X-ray reprocessing of the classical SSD model, with or without contributions from BLRs. More importantly, the continuum time delays can be comparable with the time delay between the light curves of the broad $H\beta$ emission line and the nearby optical continuum, and the latter is commonly used to calculate the BLR sizes. Hence, the BLR sizes are significantly underestimated if the continuum time delays are not properly considered. This underestimation introduces up to 0.3 dex systematic uncertainties on RM SMBH masses and BLR parallax distances. Our findings underscore that simultaneous continuum and BLR RM studies are vital for better deciphering the SMBH mass growth and the cosmological expansion history.

Keywords: Accretion (14) — Active galactic nuclei (16) — Supermassive black holes (1663) — Reverberation mapping (2019)

Corresponding author: Mouyuan Sun, Hai-Cheng Feng, Sha-Sha Li
msun88@xmu.edu.cn, hcfeng@ynao.ac.cn, lishasha@ynao.ac.cn

1. INTRODUCTION

Combining the linear and angular scales of the inner structures of active galactic nuclei (AGNs) permits

us to measure parallax distances (Elvis & Karovska 2002; Cackett et al. 2007; Wang et al. 2020; GRAVITY Collaboration et al. 2021) of supermassive black holes (SMBHs) at various redshift, thereby independently constrain the cosmological expansion history and resolve the Hubble tension (for a review, see, e.g., Di Valentino et al. 2021). The inner structures also provide valuable clues for weighing distant SMBHs (e.g., GRAVITY Collaboration et al. 2018) and constraining the SMBH-galaxy co-evolution (Kormendy & Ho 2013). However, it is very challenging to resolve AGN inner structures—the central engines and broad line regions (BLRs)—directly because of their small physical sizes (\sim light-day to light-month) and great distances from us. Fortunately, the Event Horizon Telescope has directly spatially imaged the two SMBHs, Messier 87* (Event Horizon Telescope Collaboration et al. 2019) and Sagittarius A* (Event Horizon Telescope Collaboration et al. 2022), and the spectroastrometric observations of the GRAVITY instrument on board of the Very Large Telescope Interferometer (VLTI) have resolved the BLRs for several AGNs (e.g., GRAVITY Collaboration et al. 2018). The upcoming GRAVITY+/VLTI will provide the angular scales of BLRs for a few hundred AGNs (Gravity+ Collaboration et al. 2022). Then, it is of great importance to accurately measure the linear scales of AGN inner structures.

AGN variability in all electromagnetic bands enables us to use the reverberation mapping technique (RM; Blandford & McKee 1982) to probe the linear scales of AGN inner structures in the time domain. The RM technique measures the time delays between light curves of different wavelengths (for a recent review, see Cackett et al. 2021), e.g., the time delays between broad emission lines (BELs) and the adjacent UV/optical continua measure the BLR linear scales (BLR RM), and the time delays between UV/optical continuum emission probe the SMBH accretion-disk sizes (continuum RM).

BELs produced by the photoionized BLR clouds should vary in response to the extreme ultraviolet (EUV) ionizing continuum with a light travel time delay that accounts for the BLR linear scale. However, BLR RMs often measure the time delays between the BELs and the adjacent UV/optical continua and neglect the time delay between the UV/optical and EUV emission. Recent continuum RM observations (e.g., Fausnaugh et al. 2016; Homayouni et al. 2019) indicate that the optical-EUV time delay is about three times larger than the expected light travel time of the classical standard thin disk (SSD; Shakura & Sunyaev 1973). Then, neglecting this time delay may underestimate the BLR linear-scale measurement. Quasi-simultaneous BLR and

continuum RMs are required to account for this bias if the continuum time delays change from time to time. Hence, a more thorough understanding of continuum time delays and their possible variations is still warranted.

Repeated continuum RMs for the same AGN in different flux states could offer a unique pathway for understanding the continuum time delays whose physical origin is still under active debate (e.g., Chelouche et al. 2019; Cai et al. 2018; Sun et al. 2020). Such observations can only be performed for AGNs that exhibit dramatic flux variations. NGC 4151 is a well-known local Seyfert galaxy (redshift $z = 0.00332$) with robust cosmological distance (15.8 Mpc; Yuan et al. 2020) and black-hole mass measurements (e.g., Onken et al. 2014; Roberts et al. 2021), and a favorable source of extragalactic neutrino (Abbasi et al. 2024). As shown by its 120-year long-term light curve (Oknyanskij et al. 2016), NGC 4151 has large SMBH accretion-powered continuum variations accompanied by the suppression or appearance of BELs (e.g., Sergeev et al. 2001; Li et al. 2022). In addition, Edelson et al. (2017) (hereafter E17) has performed a continuum RM observation for NGC 4151 in a low-flux state in 2016, and now the target has entered a high-flux state since 2020 (Chen et al. 2023, hereafter C23). Thus, NGC 4151 is an ideal target for repeated continuum RM studies.

We report a new continuum RM campaign with spectroscopy for NGC 4151 in a high-flux state. Combined with the historic continuum RM in a low-flux state performed by E17, we show the first direct evidence for the central engine “breathing” behavior, i.e., continuum time delays increase drastically compared with the low-flux state, which defies the classical SSD model. The “breathing” behavior adds substantial systematic uncertainties to the measurement of BLR linear size via the BLR RM, further affecting the black hole mass measurement and related cosmological studies. The manuscript is organized as follows. In Section 2, we present the observations and properties for NGC 4151 in the low- and high-flux states; in Section 3, we measure the continuum RM time delays and compare the results with the low-flux state observations and BLR RM observations; in Section 4, we show the implications of the results for AGN accretion physics, BLR sizes, black hole mass, and related cosmology; and Section 5 summaries the main conclusions.

2. OBSERVATIONS

NGC 4151 has been spectroscopically monitored over the yearly observing season, from 2022 November to 2023 July (Modified Julian Day (MJD) in 59895–60127),

using the Lijiang 2.4-m telescope in Yunnan Observatory, Chinese Academy of Sciences. The duration of observations is 232 days, and the median cadence is 2 days. The multi-band continuum light curves obtained from the spectra are shown in panel (b) of Figure 1, and the rest-frame wavelength ranges and central wavelengths are shown in Table 1. For more details on processing observational data, please refer to Appendix A.1. To our best knowledge, NGC 4151 is the first AGN for the continuum RM study with long-term and high-cadence ground-based spectroscopy. The advantages of the continuum RM with spectroscopy are twofold. First, we can simultaneously measure continuum and BEL time delays. Second, we can properly eliminate contamination from BELs in continuum RMs.

NGC 4151 is a typical changing-look AGN (CLAGN), and fortunately, E17 monitored it in a low-flux Type 1.8 state, with an $H\beta$ to $[O\ III] 5007\ \text{\AA}$ line ratio $f_{H\beta}/f_{[O\ III]} = 0.28$, while we monitored it again in a high-flux Type 1.5 state with $f_{H\beta}/f_{[O\ III]} = 0.61$. For the high-flux state in this work (the red-shaded area in Panel (a) of Figure 1), we take the average of the fluxes in rest-frame 5490–5510 \AA band as the flux f_{5500} at 5500 \AA , which has a value of $3.42 \times 10^{-14}\ \text{erg s}^{-1}\ \text{cm}^{-2}\ \text{\AA}^{-1}$ after subtracting the host galaxy contamination (Appendix A.2). The bolometric luminosity L_{bol} can be estimated using f_{5500} , combined with the distance measured by Cepheid stars (15.8 Mpc; Yuan et al. 2020) and a bolometric correction factor of 10 (Richards et al. 2006). Thus, the bolometric luminosity L_{bol} for the high-flux state is $5.61 \times 10^{43}\ \text{erg s}^{-1}$. E17 used *Swift* UVOT to monitor NGC 4151 in a low-flux state for UV/optical bands (rest-frame 1645–5781 \AA ; the blue line range in Panel (a) of Figure 3) over 69 days (MJD in 57507–57438; the blue-shaded area in Panel (a) of Figure 1) with high-frequency sampling ~ 0.2 days. The flux f_{5500} for the low-flux state is $1.04 \times 10^{-14}\ \text{erg s}^{-1}\ \text{cm}^{-2}\ \text{\AA}^{-1}$, estimated from the average flux in the V band (observed-frame 5050–5800 \AA) after subtracting the galaxy contribution. The bolometric luminosity for the low-flux state is $1.71 \times 10^{43}\ \text{erg s}^{-1}$. We did not report the measurement uncertainties of L_{bol} because the systematic uncertainties (about a factor of two; see, e.g., Richards et al. 2006) dominate the error budget. The optical-based bolometric luminosity is also consistent with the hard X-ray observations (Appendix A.3). The luminosity ratio \mathcal{R}_L between the high- and low-flux states is 3.27. The Eddington ratios $\dot{m} = L_{\text{bol}}/L_{\text{Edd}}$ are 0.003 and 0.01 for the low- and high-flux states, respectively, where $L_{\text{Edd}} = 1.26 \times 10^{38} M_{\text{BH}}/M_{\odot}\ \text{erg s}^{-1}$ is the Eddington luminosity, and $M_{\text{BH}} = 4.27 \times 10^7 M_{\odot}$ is the

black hole mass (Onken et al. 2014; Roberts et al. 2021). In summary, NGC 4151 is an ideal target for studying the accretion disk structure.

3. RESULTS

3.1. Continuum RM Analysis

3.1.1. Time delay measurements

The continuum RM technique measures the time delays between different continuum wavelengths, which probe the AGN central engine structure. We use the shortest rest-frame 4225 \AA in this work as the reference wavelength and adopt the interpolated cross-correlation analysis (via PYCCF; Sun et al. 2018) to measure the inter-band time delays with respect to the reference wavelength; the details for time delay measurements are in Appendix B. Panel (a) of Figure 2 and Table 1 show the rest-frame time delays for different wavelengths. The time delays increase with wavelengths.

We aim to quantitatively study the relationship between time delay (τ) and wavelength (λ). The fitting equation is

$$\tau = \tau_0(\lambda_0)[(\lambda/\lambda_0)^\beta - 1], \quad (1)$$

where λ_0 is the reference wavelength (i.e., 4225 \AA), $\tau_0(\lambda_0)$ and β are free parameters. The AGN SSD model has an effective temperature profile $T_{\text{eff}}(R) \propto M_{\text{BH}}^{1/4} \dot{M}^{1/4} R^{-3/4}$, where \dot{M} is the mass accretion rate. For a given wavelength λ , the corresponding characteristic radius $R(\lambda)$ is determined by $hc/\lambda = kT_{\text{eff}}(R(\lambda))$, where h is the Planck constant, c is the speed of light and k is Boltzmann constant, respectively. Then, the characteristic radius $R(\lambda) \propto M_{\text{BH}}^{1/3} \dot{M}^{1/3} \lambda^{4/3}$. Hence, we fix β to 4/3, which is a common practice in AGN continuum RM studies (e.g., E17). The panel (b) of Figure 2 shows the fitting result for Eq. 1, with the best fitting $\tau_0(4225\ \text{\AA})$ and its 1σ uncertainty being 3.72 days and 0.49 days, respectively. The reduced χ^2 of the best fit is 0.1. Thus, same as the low-flux state analyzed in E17, Eq. 1 with $\beta = 4/3$ can fit the relationship between time delays and wavelengths well.

3.1.2. Comparison with the low-flux state

NGC 4151 has continuum RM measurements for both low-flux state (E17) and high-flux state (this work). Panel (a) in Figure 3 shows the comparison of the best-fitting absolute delay (i.e., $\tau_0(\lambda_0)(\lambda/\lambda_0)^{4/3}$) for the low- and high-flux states. For the low-flux state, E17 obtained the rest-frame $\tau_0(\lambda_0) = (0.34 \pm 0.11)$ days for $\lambda_0 = 1922\ \text{\AA}$. For the high-flux state, the rest-frame $\tau_0(\lambda_0) = (3.72 \pm 0.49)$ days for $\lambda_0 = 4225\ \text{\AA}$ according to Figure 2. The continuum RM measurements in low- and high-flux states significantly differ.

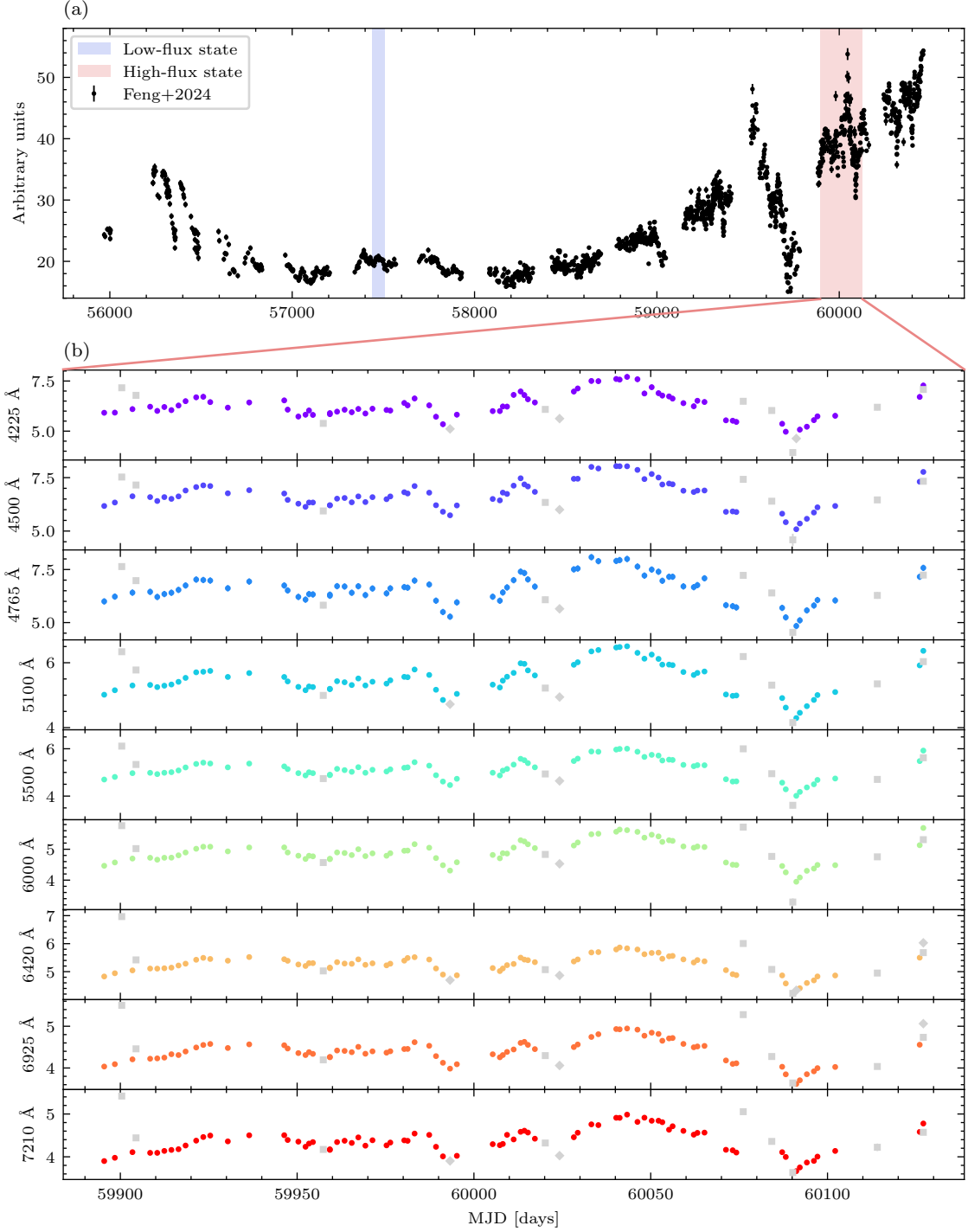


Figure 1. The multi-wavelength light curves for NGC 4151. Panel (a): the long-term light curve of NGC 4151. The black dots are the long-term light curve compiled from the Lijiang 2.4-m telescope (B band), ASAS-SN (V and g bands), and ZTF (g band) by Feng et al. 2024 (in preparation). The blue-shaded area is the period analyzed by E17 when NGC 4151 is in a low-flux state. The red-shaded area is the period analyzed in this work when NGC 4151 is in a high-flux state. Panel (b): the multi-band continuum light curves at the high-flux state. The fluxes are in units of $10^{-14} \text{ erg cm}^{-2} \text{ s}^{-1} \text{ \AA}^{-1}$. Gray squares are outliers determined by spectra and observation logs, while gray diamonds are outliers determined by a statistical method. More details can be found in Appendixes A.1 and A.4.

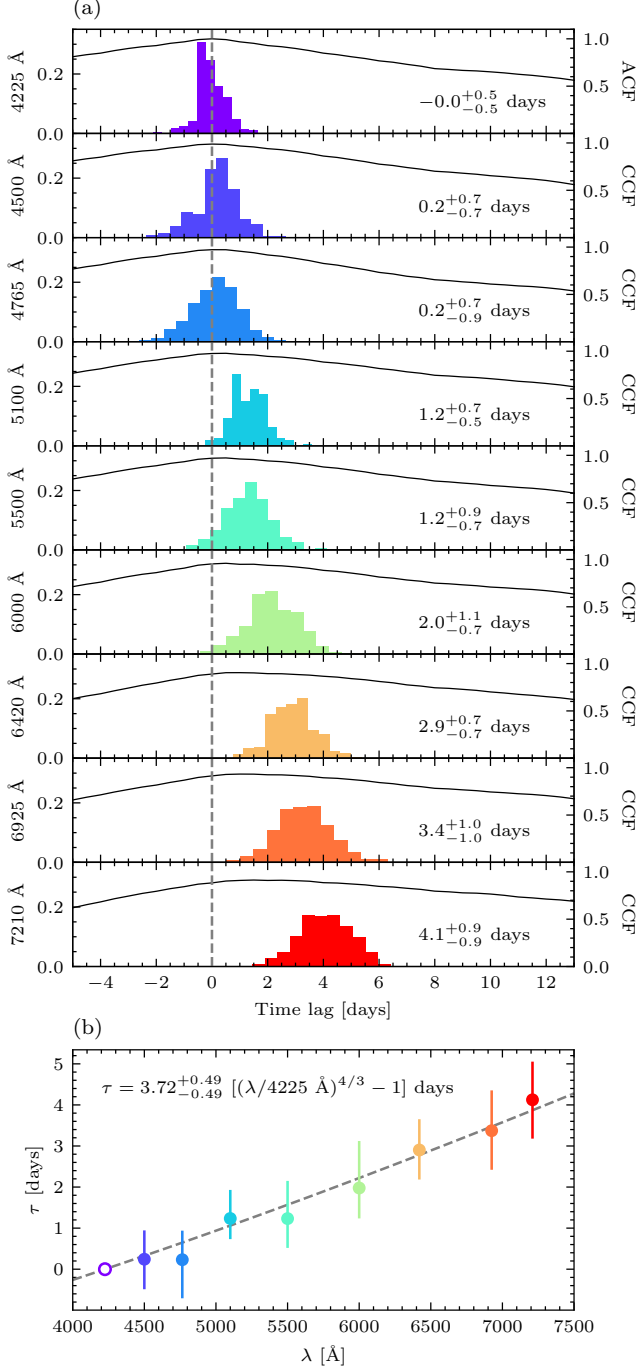


Figure 2. Rest-frame time delay measurements for different wavelengths. Panel (a): Rest-frame time delays relative to 4225 Å. The black curves are the autocorrelation function (ACF; top panel) and the interpolated cross-correlation functions (CCFs; bottom eight panels). The colored histograms are cross-correlation centroid distributions (CCCDs). The vertical dashed lines indicate zero-day delays. The rest-frame time delay and its 1σ uncertainty for each wavelength are shown in each panel. Panel (b): the fitting result of rest-frame time delays and wavelengths. The open dot is the reference wavelength 4225 Å, which is not included in the fit. The filled dots represent the time delays relative to the reference wavelength, and the error bars show their 1σ uncertainties. The grey dashed curve is the best-fitting curve, and the fitting equation is shown at the panel’s top.

Table 1. Rest-frame wavelengths and measured rest-frame time delays

Wavelength range	Central wavelength	Time delays
[Å]	[Å]	[days]
4215–4235	4225	$0.0^{+0.5}_{-0.5}$
4490–4510	4500	$0.2^{+0.7}_{-0.7}$
4755–4775	4765	$0.2^{+0.7}_{-0.9}$
5075–5125	5100	$1.2^{+0.7}_{-0.5}$
5490–5510	5500	$1.2^{+0.9}_{-0.7}$
5990–6010	6000	$2.0^{+1.1}_{-0.7}$
6410–6430	6420	$2.9^{+0.7}_{-0.7}$
6915–6935	6925	$3.4^{+1.0}_{-1.0}$
7200–7220	7210	$4.1^{+0.9}_{-0.9}$

NOTE—The first column is the rest-frame wavelength ranges used to extract fluxes from the spectra, and the second column is the rest-frame central wavelengths of wavelength ranges. The third column is the rest-frame time delays relative to 4225 Å.

One possible reason for the significant difference is that the luminosity, cadence, duration, and signal-to-noise for light curves are different for the low- and high-flux states. To quantify the impacts of these factors, we simulate light curves for both low- and high-flux states (Appendix D.1) by adopting the X-ray reprocessing of the SSD model. Given that the time delays in the low-flux state are almost six times larger than the SSD with X-ray reprocessing model predictions, we enlarge the theoretical time delay by a factor of six; this is achieved by reducing the propagation velocity of X-ray emission to one-sixth of the speed of light (hereafter the “slow” X-ray reprocessing model). The mock light curves have the same luminosity, cadence, duration, and signal-to-noise as observations in the low-flux state and high-flux state, respectively. The “slow” X-ray reprocessing model can reproduce the time delays in the low-flux state with a probability of 83%, but it is impossible to reproduce the high-flux state delays. Thus, the significant differences between the low- and high-flux delays are real and cannot be interpreted by the different properties of light curves in the two states.

For the convenience of subsequent discussions, we calculate $\tau_0(5100 \text{ \AA}) = \tau_0(\lambda_0)(5100/\lambda_0)^{4/3}$ and denote as τ_{5100} , i.e., the rest-frame time delay between the rest-frame 5100 Å and a sufficiently small wavelength (i.e., $\lambda \sim 10 \text{ \AA}$). Panel (b) in Figure 3 compares τ_{5100} for the low-flux state ($\tau_{5100,\text{low}} = 1.25 \pm 0.40$ days; dark-purple triangle) and the high-flux state ($\tau_{5100,\text{high}} =$

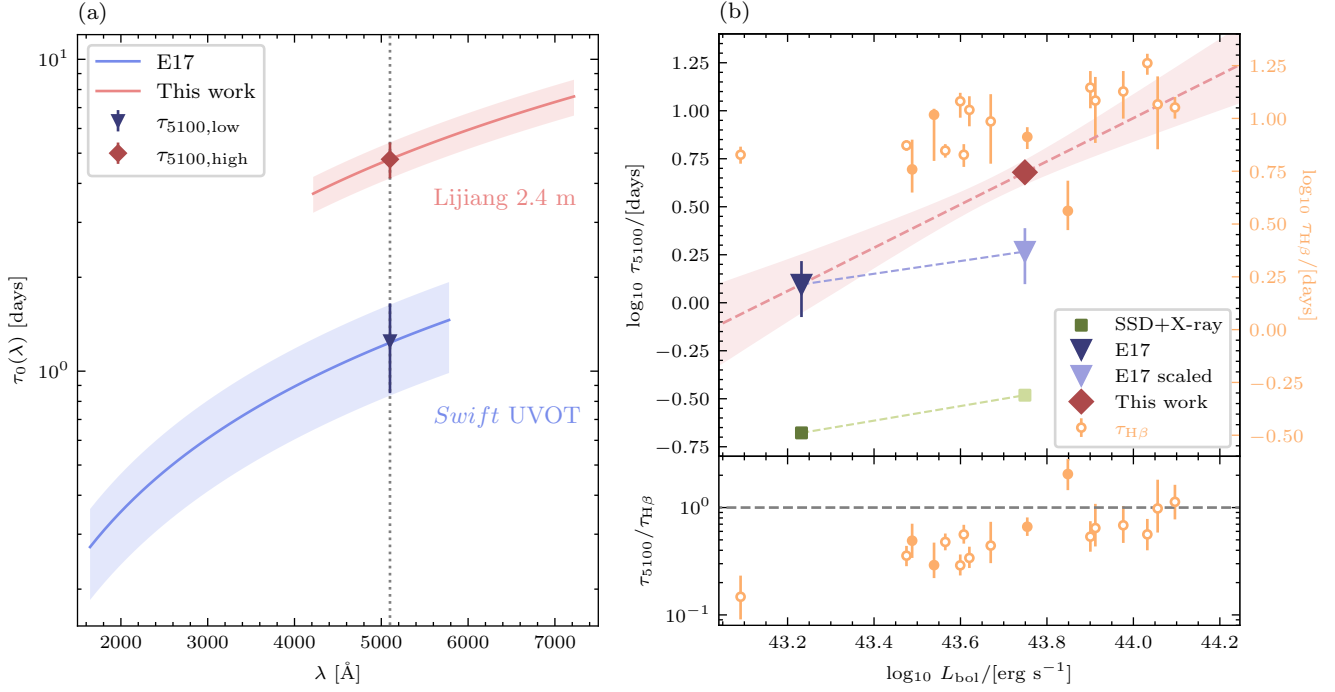


Figure 3. Time delays as a function of wavelength and luminosity. Panel (a): comparison between the rest-frame absolute delay-wavelength relations from E17 and this work, i.e., $\tau_0(\lambda) = \tau_0(\lambda_0)(\lambda/\lambda_0)^{4/3}$. The blue and red curves and shaded areas are $\tau_0(\lambda)$ - λ relation and its 1σ uncertainties for the low-flux (E17) and high-flux state (this work), respectively. The vertical dotted line corresponds to $\lambda = 5100$ Å. The dark-purple triangle and the red diamond are the low-flux state $\tau_0(5100 \text{ Å})$ ($\tau_{5100,low}$) and high-flux state $\tau_0(5100 \text{ Å})$ ($\tau_{5100,high}$), and their 1σ uncertainties. It is evident that $\tau_{5100,high}$ is larger than $\tau_{5100,low}$ by $3.8^{+1.8}_{-1.0}$ times. Panel (b): the top panel shows the evolution of τ_{5100} (left y-axis) and $\tau_{H\beta}$ (the rest-frame time delay between the rest-frame 5100 Å and H β ; right y-axis) with the bolometric luminosity L_{bol} . The dark- and light-green squares are the theoretical τ_{5100} according to the X-ray reprocessing of SSD for low- and high-flux states, respectively. The dark-purple and light-purple triangles and associated errorbars are $\tau_{5100,low}$ and the expected high-flux state τ_{5100} based on the SSD scaling relation (i.e., $\tau_{5100,low}\mathcal{R}_L^{1/3}$). The red diamond and associated errorbar are the high-flux state $\tau_{5100,high}$ and 1σ uncertainty obtained by this work. The red dashed line and shaded areas represent the best-fitting relation and the 1σ confidence interval. The open-yellow dots are historical $\tau_{H\beta}$ measurements and their 1σ uncertainties. The filled-yellow dots are for the results from Feng et al. 2024 (in preparation). The bottom panel shows the ratio $\tau_{5100}/\tau_{H\beta}$ for different bolometric luminosities. The grey dashed line indicates $\tau_{5100}/\tau_{H\beta} = 1$. It is clear that τ_{5100} can sometimes be comparable to $\tau_{H\beta}$.

4.78 ± 0.63 days; red diamond). While $\tau_{5100,low}$ is already 6.0 ± 1.9 times the prediction (dark-green square) of the SSD with X-ray reprocessing (see Appendix D.1), $\tau_{5100,high}$ is 14.9 ± 2.0 times the prediction (light-green square). Mrk 335 (Kara et al. 2023) and Fairall 9 (Edelson et al. 2024) also have repeated continuum RMs, and no time-delay variation is detected. Hence, NGC 4151 shows the largest discrepancy between the measured lags and the SSD predictions in Seyfert AGNs and is the first AGN that undergoes the accretion disk “breathing” behavior (i.e., time delays increase with luminosities).

The evolution of the AGN accretion disk structure with luminosity defies the X-ray reprocessing of the SSD model. First, according to the X-ray reprocessing of the SSD model, $\tau_0(\lambda) \propto M_{BH}^{1/3} \dot{M}^{1/3} \lambda^{4/3}$, so the prediction value of τ_{5100} in the high-flux state is $\tau_{5100,low}\mathcal{R}_L^{1/3} = 1.85 \pm 0.60$ days (light-purple triangle) is significantly

smaller than the observation. The red dashed line and shaded area in Panel (b) of Figure 3 show the best-fitting and 1σ uncertainties for the relationship between τ_{5100} and luminosity,

$$\log_{10}\left(\frac{\tau_{5100}}{\text{days}}\right) = (1.13 \pm 0.33) \log_{10}\left(\frac{L_{bol}}{\text{erg s}^{-1}}\right) - (49 \pm 14). \quad (2)$$

The slope is much steeper than the SSD model prediction. Second, the central engine shows larger-than-SSD-predicted “breathing” behavior from the low-flux state to the high-flux state in NGC 4151 within ~ 6 years. The timescale is two orders of magnitude smaller than the viscous timescale.

3.2. Comparison with the BLR RM

Optical emission (such as the 5100 Å continuum) is often used as the proxy for the ionizing continuum (such as the EUV emission) to measure the BLR locations. That

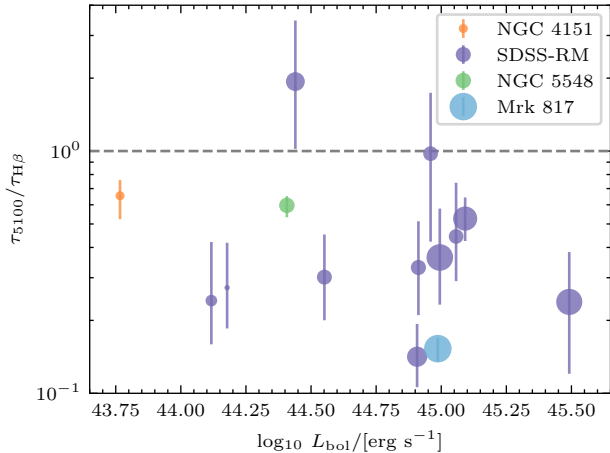


Figure 4. The ratios between τ_{5100} and $\tau_{H\beta}$ for sources with simultaneous continuum and BLR RMs. The x-axis is the bolometric luminosity on the logarithmic scale. The purple dots are the targets from the Sloan Digital Sky Survey (SDSS) RM project. The green, blue, and orange dots are NGC 5548, Mrk 817, and NGC 4151, respectively. The size of the dot increases with the Eddington ratio. τ_{5100} can be comparable to $\tau_{H\beta}$, and even larger than $\tau_{H\beta}$, so τ_{5100} cannot be ignored to obtain accurate BLR sizes. The ratio $\tau_{5100}/\tau_{H\beta}$ exhibits dispersion for different targets.

is, BLR RM observations often ignore the time delay between the ionizing continuum and the optical emission; according to the SSD model, this delay is supposed to be relatively small compared with the time delays between the optical emission and BELs. However, recent observations (e.g., Fausnaugh et al. 2016; Homayouni et al. 2019) have shown that τ_{5100} is about three times larger than the SSD prediction. NGC 4151 has a number of BLR RMs (Maoz et al. 1991; Kaspi et al. 1996; Bentz et al. 2006; De Rosa et al. 2018; Li et al. 2022, C23, and Feng et al. 2024, in preparation). We use Eq. 2 to obtain the expected τ_{5100} for each BLR RM. Surprisingly, τ_{5100} can sometimes be comparable with $\tau_{H\beta}$ —the rest-frame time delay between the rest-frame 5100 Å and H β (yellow dots in Panel (b) of Figure 3).

We collect sources with simultaneous continuum and BLR RMs (see Appendix A.5) and find that τ_{5100} can be a substantial fraction of $\tau_{H\beta}$ (Figure 4). The ratio $\tau_{5100}/\tau_{H\beta}$ exhibits a large dispersion for different targets. This leads to substantial underestimation for BLR sizes (for further discussion, see Section 4.2).

4. DISCUSSION AND PHYSICAL IMPLICATIONS

4.1. AGN accretion physics

4.1.1. AGN variability model

The SMBH accretion disk-size excess has been widely observed in continuum RM (e.g., Fausnaugh et al. 2016;

Cackett et al. 2018; Montano et al. 2022; Guo et al. 2022) and quasar microlensing studies (e.g., Morgan et al. 2010). The measured delays in continuum RMs are 2–4 times larger than the theoretical time delays of the X-ray reprocessing of the SSD model. The diffuse continuum emission on a similar scale as the BELs in BLR may influence the time delays measured by continuum RMs, especially in the Balmer jump, which has been found in some observations (e.g., Fausnaugh et al. 2016; Cackett et al. 2018; Chelouche et al. 2019). The influence should increase with the equivalent width of the broad H β , which is essentially the line-to-continuum flux ratio. The equivalent width of H β for NGC 4151 decreases with the continuum flux (for details, see Appendix A.6), which is consistent with the Baldwin effect (Baldwin 1977). Thus, the influence of the BLR diffuse continuum emission in the high-flux state is smaller than in the low-flux state, inconsistent with the significant excess of time delay in the high-flux state.

The dramatic evolution of the accretion disk with luminosity within $\lesssim 6$ years imposes a new constraint on the accretion disk model. Even with the “slow” X-ray reprocessing model, the structure transition of the accretion disk from the low-flux state to the high-flux state cannot be reproduced (Appendix D.1). The SSD model assumes blackbody radiation and an effective temperature profile $T_{\text{eff}} \propto R^{-3/4}$ (Equation D4). Hence, one solution is to modify the SSD temperature profile with some mechanisms to flatten it, increasing the sizes and light travel time delays of the emission regions for a given wavelength. Some mechanisms have been proposed to address the issue of AGN accretion disk time delay excess, e.g., the inhomogeneous disk (Dexter & Agol 2011), the windy disk (Sun et al. 2019; Li et al. 2019) and the disk embedded with stellar black holes (Zhou et al. 2024). Importantly, these mechanisms should have the potential to generate significantly different temperature profiles for the accretion disk in the low-flux state and the high-flux state to reproduce the observed τ_{5100} -luminosity relation (Figure 3). The expected timescale for the accretion disk to adjust its temperature profile is the viscous timescale, which is hundreds of years. This timescale discrepancy may seriously challenge the aforementioned mechanisms.

The inability to explain the temporal evolution of continuum time delays in NGC 4151 may imply that the popular X-ray reprocessing scenario cannot account for continuum time delays. In fact, this scenario has some weaknesses. First, there is no significant correlation between the observed X-ray and UV/optical light curves (e.g., Edelson et al. 2019). Second, this mechanism has an energy budget problem for the X-ray reprocessing

(Clavel et al. 1992; Dexter et al. 2019; Marculewicz et al. 2023; Secunda et al. 2024). Alternative AGN variability mechanisms, e.g., the inhomogeneous disk with a speculated common large-scale temperature fluctuation (Cai et al. 2018) or the corona-heated accretion-disk reprocessing model (Sun et al. 2020; Chen et al. 2024), are proposed to account for continuum time delays. In such mechanisms, the time-delay variation in NGC 4151 indicates that the thermodynamics of the central engine changes substantially (see Appendix D.2).

4.1.2. Changing-look AGN physics

The physical mechanism for changing-look behavior in CLAGNs, i.e., the appearance or disappearance of BELs over months to years, remains unclear. CLAGNs often show evident mid-infrared variations (e.g., Sheng et al. 2017), which strongly suggests that simple obscurations cannot explain the changing-look phenomenon but instead due to the intrinsic luminosity changes. The continuum RMs for NGC 4151 in both low- and high-flux states (Figure 3) suggest the accretion disk evolution is probably responsible for the luminosity variations in CLAGNs. In summary, our results impose direct evidence for accompanying accretion disk “breathing” in CLAGN manifestations.

The temporal accretion disk evolution in CLAGN provides a new way to understand its mechanism. Sniegowska et al. (2020) proposed a toy model of a narrow, unstable ring between the standard gas-dominated outer disk and the hot optically thin inner advection-dominated accretion flow (ADAF) to explain the multiple changing-look phenomena. The X-ray emission from the inner ADAF illuminates the outer disk and produces UV/optical variability. The UV/optical time delays in this scenario are similar to the X-ray reprocessing calculations in Section 3.1.2 and cannot explain the continuum RMs in the two flux states of NGC 4151. Hence, mechanisms involving strong X-ray reprocessing cannot account for the changing-look behavior in NGC 4151.

Some alternative models have been proposed to explain the changing-look phenomenon, e.g., the phenomenological model with a propagating cooling front (Ross et al. 2018), the magnetic pressure supported thick accretion disk (Dexter & Begelman 2019), the accretion disk with strong magnetic disk-outflow model (e.g., Feng et al. 2021), and the CHAR model with large magnetic fluctuations (Zhou & Sun, in preparation). These models must provide the predictions for the central engine’s “breathing” behavior. In summary, our results provide important clues to the SMBH accretion physics of highly-variable AGNs.

4.2. BLR linear sizes

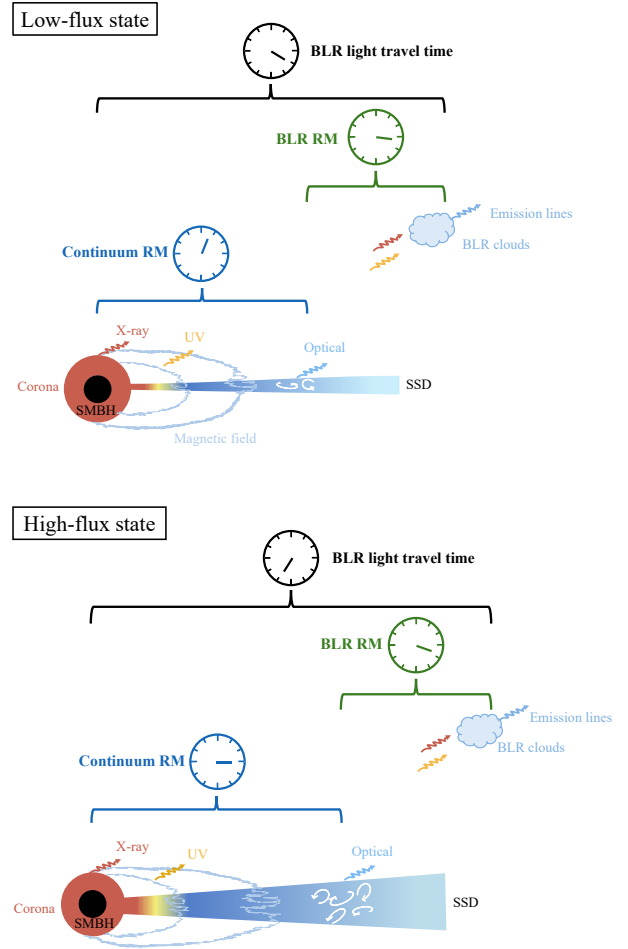


Figure 5. A schematic diagram of AGN central engine “breathing” behavior between low-flux (top panel) and high-flux (bottom panel) states. The continuum time delay (τ_{opt} ; blue clock) probes the central engine structure. The BLR clouds are ionized by EUV photons and produce emission lines. The time delays (τ_{BLR} ; black clock) between the EUV continuum and emission-line light curves probe the BLR linear sizes. Due to observational limitations, BLR RMs often measure the time delay between emission lines and their adjacent continua ($\tau_{\text{opt-BLR}}$; green clock). If $\tau_{\text{opt}} \ll \tau_{\text{opt-BLR}}$, $\tau_{\text{BLR}} \simeq \tau_{\text{opt-BLR}}$ (upper panel). However, τ_{opt} varies with luminosity significantly (lower panel), leading to large uncertainties in BLR size determinations via BLR RMs. The subsequent impacts are on black hole mass estimation and cosmological research.

In BLR RMs, optical emission is used as a proxy for the ionizing continuum. As a result, the time delay between the BEL and the ionizing continuum ($\tau_{\text{BLR}} = R_{\text{BLR}}/c$), which probes the real BLR size

(R_{BLR}), should be

$$\tau_{\text{BLR}} = \tau_{\text{opt}} + \tau_{\text{opt-BLR}} = \tau_{\text{opt-BLR}}(\tau_{\text{opt}}/\tau_{\text{opt-BLR}} + 1), \quad (3)$$

where τ_{opt} and $\tau_{\text{opt-BLR}}$ are the continuum time delay between ionizing continuum and optical emission and the time delay between the optical emission and the BEL, respectively. The two time delays can be measured via the continuum and BLR RMs (Figure 5), respectively. As shown in Figures 3 and 4, τ_{opt} can be comparable to $\tau_{\text{opt-BLR}}$, causing the BLR linear scales to be occasionally underestimated by $\lesssim 0.3$ dex. This underestimation may contribute substantially to the scatter in the AGN R_{BLR} -luminosity relation (Bentz et al. 2013; Du et al. 2014), and the latter is fundamental to the widely-used single-epoch virial SMBH mass estimators.

4.3. Black hole mass measurement

The location and velocity of BLR clouds can probe the central SMBH mass. If the BLR clouds are virialized, the virial mass of the central SMBH is

$$M_{\text{BH}} = f \frac{c\tau_{\text{BLR}}(\Delta V)^2}{G}, \quad (4)$$

where f is a dimensionless virial factor that includes the unknown geometries and kinematics of the BLR clouds, ΔV is the BLR cloud velocity as represented by the line widths of the broad emission lines, and G is the gravitational constant. As mentioned in Section 4.2, BLR RMs use $\tau_{\text{opt-BLR}}$ to represent τ_{BLR} . The measured M_{BH} will be underestimated by a factor of $(\tau_{\text{opt}}/\tau_{\text{opt-BLR}} + 1)$, where $\tau_{\text{opt}}/\tau_{\text{opt-BLR}}$ varies with luminosity for the same target (Figure 3). At low luminosities, τ_{opt} can be ignored, while at high luminosities, τ_{opt} plays an important role since $\tau_{\text{opt}}/\tau_{\text{opt-BLR}} \simeq 1$ for NGC 4151, and the corresponding underestimation of the SMBH mass is ~ 0.3 dex (we will demonstrate this effect in a future study). Thus, the simultaneous continuum RM and BLR RM are necessary to improve the precision of SMBH mass measurements.

4.4. BLR time delay cosmology

The linear scale of the BLR is crucial for the accurate measurement of cosmological parameters using the quasar R_{BLR} -luminosity relation (e.g., Watson et al. 2011). The idea relies on the observed relation between $\tau_{\text{opt-BLR}}$ and the optical luminosity L_{opt} , $\tau_{\text{opt-BLR}} \propto L_{\text{opt}}^{0.53}$ (e.g., Bentz et al. 2013). However, recent BLR RM studies reveal that the R_{BLR} -luminosity relation shows large dispersion for high accretion rate targets (e.g., Du et al. 2014; Shen et al. 2024). Meanwhile, multiple BLR RM observations for the same target also show discrepancies in the relationship between $\tau_{\text{opt-BLR}}$ and L_{opt}

(e.g., Figure 9 in C23 and Figure 13 in Pei et al. 2017). The dispersion may be caused by the different spectral energy distributions for the same luminosity, resulting in different ionizing continua (e.g., Wu et al. 2024). Our results reveal a new possibility. The ratio $\tau_{\text{opt}}/\tau_{\text{opt-BLR}}$ varies significantly (Figure 3), resulting large dispersion between τ_{BLR} and $\tau_{\text{opt-BLR}}$. Therefore, the continuum time delays induce significant systematic uncertainties in using the R_{BLR} -luminosity relation to measure single-epoch virial BH mass and cosmological parameters.

The angular size (θ) and linear size ($R_{\text{BLR}} = c\tau_{\text{BLR}}$) of BLR provide a new parallax method to measure the angular distances (D_{A}) of quasars and subsequently measure cosmology model parameters (Elvis & Karovska 2002). Wang et al. (2020) first measured the angular distance for 3C 273 and constrained the Hubble constant H_0 , using the angular size measured by spectroastrometry of GRAVITY observations (GRAVITY Collaboration et al. 2018) and the linear size ($c\tau_{\text{opt-BLR}}$) measured by the BLR RM. Our result suggests that the observed linear size by BLR RM significantly underestimates the actual BLR size (Figure 5), which introduces new systematic uncertainties in the angular distance measurement, especially in high-flux states. It is therefore necessary to measure τ_{opt} , $\tau_{\text{opt-BLR}}$, and the BLR angular size simultaneously in the low- and high-flux states, respectively.

4.5. Gravitational lensing cosmology

When a distant quasar is lensed into multiple images by a massive foreground galaxy, the time delay of the flux variations between different images is often used to study cosmological models. The Hubble constant H_0 measured by the strong gravitational lensing method has reached a precision of 2.4% (e.g., Wong et al. 2020). Microlensing caused by stars in the foreground galaxy is one of the sources of uncertainty. The effect of microlensing on the time delay between two images results from the inclination of the accretion disk in the line of sight and the different magnifications of stars in different emission regions of the accretion disk (Tie & Kochanek 2018). The time delay between different emission regions of the accretion disk determines the influence of microlensing on strong-lensing time delays. Our results show that the time delay for NGC 4151 in the high-flux state is 14.9 ± 2.0 times the SSD model prediction, which can also occur in strong gravitational lensing quasars. The unknown time delay in the emission regions of the accretion disk of strong gravitational lensing quasars introduces an unavoidable uncertainty in gravitational lensing cosmology.

5. SUMMARY

We have carried out a 232-day-long ~ 2 -day-cadence spectroscopic RM campaign NGC 4151 in the high-flux state. Comparing our results with those in the low-flux state by E17, we have given direct evidence for central engine “breathing” behavior for the first time. The main conclusions are summarized below.

1. We have measured the continuum RM time delays for NGC 4151 in the high-flux state (see Section 3.1.1; Figure 2). Our results are 14.9 ± 2.0 times larger than the SSD with X-ray reprocessing model prediction (Figure 3). This is the largest discrepancy detected between the observed time lags and the model predictions.
2. Our time lags in the high-flux state are $3.8_{-1.0}^{+1.8}$ times larger than those in the low-flux state (see Section 3.1.2; Figure 3). The significant central engine “breathing” behavior defies the X-ray reprocessing of the SSD model and challenges other models (see Section 4.1.1).
3. The changing-look behavior in AGN accompanied by temporal accretion disk structure evolution provides new insight into the underlying physical mechanisms of CLAGNs and rules out models involved with strong X-ray reprocessing (see Section 4.1.2).
4. Our continuum RM implies that the time delay between optical and ionizing emission varies significantly and can be ~ 14.9 times larger than the theoretical expectation. This introduces substantial systematic uncertainties in measuring the BLR linear scales via the BLR RM (see Section 4.2; Figure 5). Hence, the continuum time delay will seriously limit the precision of the BLR black-hole mass estimation (see Section 4.3), the BLR parallax cosmology (see Section 4.4), and gravitational lensing cosmology (see Section 4.5).

We acknowledge S.Y., S.S.W., Y.X.P., and Y.C.Z. for their helpful discussion. We acknowledge support from the National Key R&D Program of China (No. 2023YFA1607903 and 2021YFA1600404). S.Y.Z. and M.Y.S. acknowledge support from the National Natural Science Foundation of China (NSFC-12322303), and the Natural Science Foundation of Fujian Province of China (No. 2022J06002). H.C.F. acknowledges support from National Natural Science Foundation of China (NSFC-12203096), Yunnan Fundamental Research Projects (grant NO. 202301AT070339), and Special Research Assistant Funding Project of Chinese Academy of Sciences. S.S.L. acknowledges support from National Natural Science Foundation of China (NSFC-12303022), Yunnan Fundamental Research Projects (grant NO. 202301AT070358), and Yunnan Postdoctoral Research Foundation Funding Project. Y.Q.X. acknowledges support from the National Natural Science Foundation of China (NSFC-12025303 and 12393814). J.X.W. acknowledges support from the National Natural Science Foundation of China (NSFC-12033006 & 12192221). J.M.B. acknowledges support from National Natural Science Foundation of China (NSFC-11991051), H.T.L. acknowledges support from National Natural Science Foundation of China (NSFC-12373018), K.X.L. acknowledges financial support from the National Natural Science Foundation of China (NSFC-12073068), the Youth Innovation Promotion Association of Chinese Academy of Sciences (2022058), and the Young Talent Project of Yunnan Province. We acknowledge the support of the staff of the Lijiang 2.4 m telescope. Funding for the telescope has been provided by Chinese Academy of Sciences and the People’s Government of Yunnan Province.

Facility: YAO:2.4m

Software: Matplotlib (Hunter 2007), Numpy (Harris et al. 2020), Scipy (Virtanen et al. 2020), Astropy (Astropy Collaboration et al. 2013), emcee (Foreman-Mackey et al. 2013), PYCCF (Sun et al. 2018), statsmodels (Seabold & Perktold 2010), astroML (Vanderplas et al. 2012)

REFERENCES

- Abbasi, R., Ackermann, M., Adams, J., et al. 2024, arXiv e-prints, arXiv:2406.06684, doi: 10.48550/arXiv.2406.06684
- Astropy Collaboration, Robitaille, T. P., Tollerud, E. J., et al. 2013, *A&A*, 558, A33, doi: 10.1051/0004-6361/201322068
- Baldwin, J. A. 1977, *ApJ*, 214, 679, doi: 10.1086/155294
- Bentz, M. C., & Katz, S. 2015, *PASP*, 127, 67, doi: 10.1086/679601
- Bentz, M. C., Denney, K. D., Cackett, E. M., et al. 2006, *ApJ*, 651, 775, doi: 10.1086/507417

- Bentz, M. C., Denney, K. D., Grier, C. J., et al. 2013, *ApJ*, 767, 149, doi: [10.1088/0004-637X/767/2/149](https://doi.org/10.1088/0004-637X/767/2/149)
- Blandford, R. D., & McKee, C. F. 1982, *ApJ*, 255, 419, doi: [10.1086/159843](https://doi.org/10.1086/159843)
- Cackett, E. M., Bentz, M. C., & Kara, E. 2021, *iScience*, 24, 102557, doi: [10.1016/j.isci.2021.102557](https://doi.org/10.1016/j.isci.2021.102557)
- Cackett, E. M., Chiang, C.-Y., McHardy, I., et al. 2018, *ApJ*, 857, 53, doi: [10.3847/1538-4357/aab4f7](https://doi.org/10.3847/1538-4357/aab4f7)
- Cackett, E. M., Horne, K., & Winkler, H. 2007, *MNRAS*, 380, 669, doi: [10.1111/j.1365-2966.2007.12098.x](https://doi.org/10.1111/j.1365-2966.2007.12098.x)
- Cai, Z.-Y., Wang, J.-X., Zhu, F.-F., et al. 2018, *ApJ*, 855, 117, doi: [10.3847/1538-4357/aab091](https://doi.org/10.3847/1538-4357/aab091)
- Chelouche, D., Pozo Nuñez, F., & Kaspi, S. 2019, *Nature Astronomy*, 3, 251, doi: [10.1038/s41550-018-0659-x](https://doi.org/10.1038/s41550-018-0659-x)
- Chen, J., Sun, M., & Zhang, Z.-X. 2024, *ApJ*, 962, 134, doi: [10.3847/1538-4357/ad16ea](https://doi.org/10.3847/1538-4357/ad16ea)
- Chen, Y.-J., Bao, D.-W., Zhai, S., et al. 2023, *MNRAS*, 520, 1807, doi: [10.1093/mnras/stad051](https://doi.org/10.1093/mnras/stad051)
- Clavel, J., Nandra, K., Makino, F., et al. 1992, *ApJ*, 393, 113, doi: [10.1086/171490](https://doi.org/10.1086/171490)
- Das, V., Crenshaw, D. M., Hutchings, J. B., et al. 2005, *AJ*, 130, 945, doi: [10.1086/432255](https://doi.org/10.1086/432255)
- De Rosa, G., Fausnaugh, M. M., Grier, C. J., et al. 2018, *ApJ*, 866, 133, doi: [10.3847/1538-4357/aadd11](https://doi.org/10.3847/1538-4357/aadd11)
- Dexter, J., & Agol, E. 2011, *ApJL*, 727, L24, doi: [10.1088/2041-8205/727/1/L24](https://doi.org/10.1088/2041-8205/727/1/L24)
- Dexter, J., & Begelman, M. C. 2019, *MNRAS*, 483, L17, doi: [10.1093/mnrasl/sly213](https://doi.org/10.1093/mnrasl/sly213)
- Dexter, J., Xin, S., Shen, Y., et al. 2019, *ApJ*, 885, 44, doi: [10.3847/1538-4357/ab4354](https://doi.org/10.3847/1538-4357/ab4354)
- Di Valentino, E., Mena, O., Pan, S., et al. 2021, *Classical and Quantum Gravity*, 38, 153001, doi: [10.1088/1361-6382/ac086d](https://doi.org/10.1088/1361-6382/ac086d)
- Du, P., Hu, C., Lu, K.-X., et al. 2014, *ApJ*, 782, 45, doi: [10.1088/0004-637X/782/1/45](https://doi.org/10.1088/0004-637X/782/1/45)
- Edelson, R., Peterson, B. M., Gelbord, J., et al. 2024, *arXiv e-prints*, arXiv:2407.09445, doi: [10.48550/arXiv.2407.09445](https://doi.org/10.48550/arXiv.2407.09445)
- Edelson, R., Gelbord, J., Cackett, E., et al. 2017, *ApJ*, 840, 41, doi: [10.3847/1538-4357/aa6890](https://doi.org/10.3847/1538-4357/aa6890)
- . 2019, *ApJ*, 870, 123, doi: [10.3847/1538-4357/aaf3b4](https://doi.org/10.3847/1538-4357/aaf3b4)
- Elvis, M., & Karovska, M. 2002, *ApJL*, 581, L67, doi: [10.1086/346015](https://doi.org/10.1086/346015)
- Evans, P. A., Beardmore, A. P., Page, K. L., et al. 2007, *A&A*, 469, 379, doi: [10.1051/0004-6361:20077530](https://doi.org/10.1051/0004-6361:20077530)
- Event Horizon Telescope Collaboration, Akiyama, K., Alberdi, A., et al. 2019, *ApJL*, 875, L4, doi: [10.3847/2041-8213/ab0e85](https://doi.org/10.3847/2041-8213/ab0e85)
- . 2022, *ApJL*, 930, L14, doi: [10.3847/2041-8213/ac6429](https://doi.org/10.3847/2041-8213/ac6429)
- Fausnaugh, M. M., Denney, K. D., Barth, A. J., et al. 2016, *ApJ*, 821, 56, doi: [10.3847/0004-637X/821/1/56](https://doi.org/10.3847/0004-637X/821/1/56)
- Feng, J., Cao, X., Li, J.-w., & Gu, W.-M. 2021, *ApJ*, 916, 61, doi: [10.3847/1538-4357/ac07a6](https://doi.org/10.3847/1538-4357/ac07a6)
- Foreman-Mackey, D., Hogg, D. W., Lang, D., & Goodman, J. 2013, *PASP*, 125, 306, doi: [10.1086/670067](https://doi.org/10.1086/670067)
- GRAVITY Collaboration, Sturm, E., Dexter, J., et al. 2018, *Nature*, 563, 657, doi: [10.1038/s41586-018-0731-9](https://doi.org/10.1038/s41586-018-0731-9)
- GRAVITY Collaboration, Amorim, A., Bauböck, M., et al. 2021, *A&A*, 654, A85, doi: [10.1051/0004-6361/202141426](https://doi.org/10.1051/0004-6361/202141426)
- Gravity+ Collaboration, Abuter, R., Alarcon, P., et al. 2022, *The Messenger*, 189, 17, doi: [10.18727/0722-6691/5285](https://doi.org/10.18727/0722-6691/5285)
- Grier, C. J., Trump, J. R., Shen, Y., et al. 2017, *ApJ*, 851, 21, doi: [10.3847/1538-4357/aa98dc](https://doi.org/10.3847/1538-4357/aa98dc)
- Guo, H., Barth, A. J., & Wang, S. 2022, *ApJ*, 940, 20, doi: [10.3847/1538-4357/ac96ec](https://doi.org/10.3847/1538-4357/ac96ec)
- Harris, C. R., Millman, K. J., van der Walt, S. J., et al. 2020, *Nature*, 585, 357–362, doi: [10.1038/s41586-020-2649-2](https://doi.org/10.1038/s41586-020-2649-2)
- Homayouni, Y., Trump, J. R., Grier, C. J., et al. 2019, *ApJ*, 880, 126, doi: [10.3847/1538-4357/ab2638](https://doi.org/10.3847/1538-4357/ab2638)
- Hunter, J. D. 2007, *Computing in Science and Engineering*, 9, 90, doi: [10.1109/MCSE.2007.55](https://doi.org/10.1109/MCSE.2007.55)
- Kara, E., Mehdipour, M., Kriss, G. A., et al. 2021, *ApJ*, 922, 151, doi: [10.3847/1538-4357/ac2159](https://doi.org/10.3847/1538-4357/ac2159)
- Kara, E., Barth, A. J., Cackett, E. M., et al. 2023, *ApJ*, 947, 62, doi: [10.3847/1538-4357/acbcd3](https://doi.org/10.3847/1538-4357/acbcd3)
- Kaspi, S., Maoz, D., Netzer, H., et al. 1996, *ApJ*, 470, 336, doi: [10.1086/177870](https://doi.org/10.1086/177870)
- Kelly, B. C., Bechtold, J., & Siemiginowska, A. 2009, *ApJ*, 698, 895, doi: [10.1088/0004-637X/698/1/895](https://doi.org/10.1088/0004-637X/698/1/895)
- King, A. R., Pringle, J. E., & Livio, M. 2007, *MNRAS*, 376, 1740, doi: [10.1111/j.1365-2966.2007.11556.x](https://doi.org/10.1111/j.1365-2966.2007.11556.x)
- Kormendy, J., & Ho, L. C. 2013, *ARA&A*, 51, 511, doi: [10.1146/annurev-astro-082708-101811](https://doi.org/10.1146/annurev-astro-082708-101811)
- Krolik, J. H., Horne, K., Kallman, T. R., et al. 1991, *ApJ*, 371, 541, doi: [10.1086/169918](https://doi.org/10.1086/169918)
- Li, S.-S., Feng, H.-C., Liu, H. T., et al. 2022, *ApJ*, 936, 75, doi: [10.3847/1538-4357/ac8745](https://doi.org/10.3847/1538-4357/ac8745)
- Li, T., Sun, M., Xu, X., et al. 2021, *ApJL*, 912, L29, doi: [10.3847/2041-8213/abf9aa](https://doi.org/10.3847/2041-8213/abf9aa)
- Li, Y.-P., Yuan, F., & Dai, X. 2019, *MNRAS*, 483, 2275, doi: [10.1093/mnras/sty3245](https://doi.org/10.1093/mnras/sty3245)
- Maoz, D., Netzer, H., Mazeh, T., et al. 1991, *ApJ*, 367, 493, doi: [10.1086/169646](https://doi.org/10.1086/169646)
- Marculewicz, M., Sun, M., Wu, J., & Zhang, Z. 2023, *ApJ*, 956, 126, doi: [10.3847/1538-4357/acf312](https://doi.org/10.3847/1538-4357/acf312)
- Montano, J. W., Guo, H., Barth, A. J., et al. 2022, *ApJL*, 934, L37, doi: [10.3847/2041-8213/ac7e54](https://doi.org/10.3847/2041-8213/ac7e54)

- Morgan, C. W., Kochanek, C. S., Morgan, N. D., & Falco, E. E. 2010, *ApJ*, 712, 1129, doi: [10.1088/0004-637X/712/2/1129](https://doi.org/10.1088/0004-637X/712/2/1129)
- Oknyanskij, V. L., Metlova, N. V., Huseynov, N. A., Guo, D.-F., & Lyuty, V. M. 2016, *Odessa Astronomical Publications*, 29, 95, doi: [10.18524/1810-4215.2016.29.85058](https://doi.org/10.18524/1810-4215.2016.29.85058)
- Onken, C. A., Valluri, M., Brown, J. S., et al. 2014, *ApJ*, 791, 37, doi: [10.1088/0004-637X/791/1/37](https://doi.org/10.1088/0004-637X/791/1/37)
- Pei, L., Fausnaugh, M. M., Barth, A. J., et al. 2017, *ApJ*, 837, 131, doi: [10.3847/1538-4357/aa5eb1](https://doi.org/10.3847/1538-4357/aa5eb1)
- Peterson, B. M., Wanders, I., Horne, K., et al. 1998, *PASP*, 110, 660, doi: [10.1086/316177](https://doi.org/10.1086/316177)
- Ricci, C., Trakhtenbrot, B., Koss, M. J., et al. 2017, *ApJS*, 233, 17, doi: [10.3847/1538-4365/aa96ad](https://doi.org/10.3847/1538-4365/aa96ad)
- Richards, G. T., Lacy, M., Storrie-Lombardi, L. J., et al. 2006, *ApJS*, 166, 470, doi: [10.1086/506525](https://doi.org/10.1086/506525)
- Roberts, C. A., Bentz, M. C., Vasiliev, E., Valluri, M., & Onken, C. A. 2021, *ApJ*, 916, 25, doi: [10.3847/1538-4357/ac05b6](https://doi.org/10.3847/1538-4357/ac05b6)
- Ross, N. P., Ford, K. E. S., Graham, M., et al. 2018, *MNRAS*, 480, 4468, doi: [10.1093/mnras/sty2002](https://doi.org/10.1093/mnras/sty2002)
- Seabold, S., & Perktold, J. 2010, in *9th Python in Science Conference*
- Secunda, A., Jiang, Y.-F., & Greene, J. E. 2024, *ApJL*, 965, L29, doi: [10.3847/2041-8213/ad34b0](https://doi.org/10.3847/2041-8213/ad34b0)
- Sergeev, S. G., Pronik, V. I., & Sergeeva, E. A. 2001, *ApJ*, 554, 245, doi: [10.1086/321382](https://doi.org/10.1086/321382)
- Shakura, N. I., & Sunyaev, R. A. 1973, *A&A*, 24, 337
- Shen, Y., Greene, J. E., Ho, L. C., et al. 2015, *ApJ*, 805, 96, doi: [10.1088/0004-637X/805/2/96](https://doi.org/10.1088/0004-637X/805/2/96)
- Shen, Y., Grier, C. J., Horne, K., et al. 2024, *ApJS*, 272, 26, doi: [10.3847/1538-4365/ad3936](https://doi.org/10.3847/1538-4365/ad3936)
- Sheng, Z., Wang, T., Jiang, N., et al. 2017, *ApJL*, 846, L7, doi: [10.3847/2041-8213/aa85de](https://doi.org/10.3847/2041-8213/aa85de)
- Sniegowska, M., Czerny, B., Bon, E., & Bon, N. 2020, *A&A*, 641, A167, doi: [10.1051/0004-6361/202038575](https://doi.org/10.1051/0004-6361/202038575)
- Sun, M., Grier, C. J., & Peterson, B. M. 2018, *PyCCF: Python Cross Correlation Function for reverberation mapping studies*, *Astrophysics Source Code Library*, record ascl:1805.032
- Sun, M., Xue, Y., Trump, J. R., & Gu, W.-M. 2019, *MNRAS*, 482, 2788, doi: [10.1093/mnras/sty2885](https://doi.org/10.1093/mnras/sty2885)
- Sun, M., Xue, Y., Brandt, W. N., et al. 2020, *ApJ*, 891, 178, doi: [10.3847/1538-4357/ab789e](https://doi.org/10.3847/1538-4357/ab789e)
- Tie, S. S., & Kochanek, C. S. 2018, *MNRAS*, 473, 80, doi: [10.1093/mnras/stx2348](https://doi.org/10.1093/mnras/stx2348)
- Vanderplas, J., Connolly, A., Ivezić, Ž., & Gray, A. 2012, in *Conference on Intelligent Data Understanding (CIDU)*, 47–54, doi: [10.1109/CIDU.2012.6382200](https://doi.org/10.1109/CIDU.2012.6382200)
- Virtanen, P., Gommers, R., Oliphant, T. E., et al. 2020, *Nature Methods*, 17, 261, doi: [10.1038/s41592-019-0686-2](https://doi.org/10.1038/s41592-019-0686-2)
- Wang, J.-M., Songsheng, Y.-Y., Li, Y.-R., Du, P., & Zhang, Z.-X. 2020, *Nature Astronomy*, 4, 517, doi: [10.1038/s41550-019-0979-5](https://doi.org/10.1038/s41550-019-0979-5)
- Watson, D., Denney, K. D., Vestergaard, M., & Davis, T. M. 2011, *ApJL*, 740, L49, doi: [10.1088/2041-8205/740/2/L49](https://doi.org/10.1088/2041-8205/740/2/L49)
- Winkler, H. 1992, *MNRAS*, 257, 677, doi: [10.1093/mnras/257.4.677](https://doi.org/10.1093/mnras/257.4.677)
- Wong, K. C., Suyu, S. H., Chen, G. C. F., et al. 2020, *MNRAS*, 498, 1420, doi: [10.1093/mnras/stz3094](https://doi.org/10.1093/mnras/stz3094)
- Wu, Q., Shen, Y., Guo, H., et al. 2024, *arXiv e-prints*, arXiv:2407.01737, doi: [10.48550/arXiv.2407.01737](https://doi.org/10.48550/arXiv.2407.01737)
- Yan, R., Chen, Y., Lazarz, D., et al. 2019, *ApJ*, 883, 175, doi: [10.3847/1538-4357/ab3ebc](https://doi.org/10.3847/1538-4357/ab3ebc)
- Yang, S., Du, P., & Wang, J.-M. 2024, *arXiv e-prints*, arXiv:2407.04257, doi: [10.48550/arXiv.2407.04257](https://doi.org/10.48550/arXiv.2407.04257)
- Yuan, W., Fausnaugh, M. M., Hoffmann, S. L., et al. 2020, *ApJ*, 902, 26, doi: [10.3847/1538-4357/abb377](https://doi.org/10.3847/1538-4357/abb377)
- Zhou, S., Sun, M., Liu, T., et al. 2024, *ApJL*, 966, L9, doi: [10.3847/2041-8213/ad3c3f](https://doi.org/10.3847/2041-8213/ad3c3f)

APPENDIX

A. OBSERVATION DATA PROCESSING

A.1. *Light curve extraction*

Observations of NGC 4151 were conducted using the Yunnan Faint Object Spectrograph and Camera mounted on the 2.4-m telescope at Lijiang. The specific observation mode utilized Grism 14 with a slit width of $5''.05$, and an additional UV-blocking filter was employed to cut off light with wavelengths below 4150 \AA , thereby reducing the impact of second-order spectra. A long slit was used, which allows for simultaneous observation of the target and comparison star. This setup facilitates accurate flux calibration by using the comparison star. In this observation mode, the spectral dispersion is 1.8 \AA/pixel , covering a wavelength range from 4193 \AA to 7374 \AA (see Feng et al. 2024, in preparation, for more details).

The raw data are processed using the standard procedures in PyRAF¹, with an extraction aperture of $8''.49$ and background region of $14''.15$ to $19''.81$. The flux calibration process involves several key steps: first, the comparison star is calibrated using observations of standard stars taken under good weather conditions to generate an initial template spectrum. This template is then matched against spectra from a stellar template library (Yan et al. 2019), selecting the spectrum with the smallest fitting residuals as the standard template. Using this standard template, along with the daily spectra of the comparison star, we perform flux calibration and atmospheric absorption correction on the target, obtaining the final flux-calibrated spectra.

Additionally, we correct for galactic extinction and the redshift of each spectrum. To extract continuum light curves, we select nine line-free continuum windows (as shown in Table 1). The median and standard error of the spectral data within each window are used as the measurement values and errors, respectively, thus deriving the light curve for each bin.

A.2. *Host galaxy contribution*

Starlight from the host galaxy is mixed into the observed flux and should be properly subtracted. Yang et al. (2024) performed the image decomposition for NGC 4151 using the *Hubble Space Telescope* high-resolution images. Then, they obtained the host galaxy flux at 5500 \AA for a circular aperture of 5 arcsec (corresponding to the Swift observations) and the $5''.05 \times 8''.49$ aperture (for the spectroscopic observations in this work). The corresponding host galaxy fluxes are $2.11 \times 10^{-14} \text{ erg s}^{-1} \text{ cm}^{-2} \text{ \AA}^{-1}$ and $1.73 \times 10^{-14} \text{ erg s}^{-1} \text{ cm}^{-2} \text{ \AA}^{-1}$, respectively (Yang et al., private communication).

A.3. *Swift/XRT observations*

NGC 4151 was frequently observed by the XRT on board *Swift*. To obtain the X-ray light curve that covers the low- and high-flux states of NGC 4151, we consider the *Swift*/XRT observations with the target IDs 00034455 and 00096883. The XRT light curve is built via the UK Swift Science Data Centre online tool (Evans et al. 2007). We calculate the median XRT count rates for the MJD ranges [57438, 57507] (the low-flux state) and [59890, 60100] (the high-flux state), respectively. The 0.3-10 keV median count rates for the two states are $1.03 \pm 0.02 \text{ counts s}^{-1}$ and $1.7 \pm 0.1 \text{ counts s}^{-1}$, respectively. Hence, the X-ray flux varies by a factor of 1.65 ± 0.07 , which can cause the disk size to increase by a factor of $1.65^{1/3} = 1.18$ for the X-ray reprocessing of an SSD (Eq. D5).

NGC 4151 is also included in the *Swift*/BAT 70-month AGN Catalog with the intrinsic 14–195 keV luminosity of $10^{43.1} \text{ erg s}^{-1}$ (Ricci et al. 2017). The ratio of the X-ray to disk luminosities is $\simeq 20\%$. Therefore, X-ray illumination should not be the main energy source for disk emission.

A.4. *Outliers*

Variations due to “problematic” observations rather than intrinsic fluctuations in the SMBH accretion disk can bias the time delay measurements. We first smooth light curves using a smoothing function `lowess`², and obtain the

¹ <https://github.com/iraf-community/pyraf>

² https://www.statsmodels.org/devel/generated/statsmodels.nonparametric.smoothers_lowess.lowess

normalized median absolute deviation σ_{1c} of the residuals of the smoothed and the original light curves. The statistical outliers are points that deviate from the smoothed light curve with $3\sigma_{1c}$. To further determine the reliability of the outliers, we check the spectra and observation logs and find some problematic spectra with poor weather conditions or instrumental issues (the gray squares in Figure 1. (b)). It turns out that some statistical outliers also correspond to such problematic spectroscopic observations. The remaining statistical outliers (gray diamonds in Figure 1. (b)) have substantial deviations between photometric and spectroscopic fluxes.

A.5. Archival data

We compile sources with simultaneous measurements of τ_{5100} and $\tau_{H\beta}$ (Figure 4). The sample consists of the SDSS-RM targets, NGC 5548, Mrk 817, and NGC 4151 (this work).

SDSS – RM targets—The bolometric luminosities are estimated from the 5100 Å monochromatic luminosity measured by Shen et al. (2015) and a bolometric correction factor 10 (Richards et al. 2006). The Eddington ratios can be estimated by the bolometric luminosity and the black hole mass measured by Shen et al. (2015). Homayouni et al. (2019) measure the observed-frame time delays τ_{i-g} between g band and i band. According to Eq. 1, we can convert τ_{g-i} to τ_{5100} by

$$\tau_{5100} = \tau_{i-g}(1+z)^{1/3}[(\lambda_i/5100 \text{ \AA})^{4/3} - ((\lambda_g/5100 \text{ \AA})^{4/3})]^{-1}, \quad (\text{A1})$$

where z is the redshift, $\lambda_i = 7625 \text{ \AA}$ and $\lambda_g = 4770 \text{ \AA}$ are the observed-frame central wavelengths for i and g bands, respectively. Grier et al. (2017) measure the rest-frame time delays $\tau_{\text{con-H}\beta}$ between the $g+i$ (they combine the light curves of the g and i bands for inter-calibration) emission and the broad $H\beta$. We estimate $\tau_{H\beta}$ (i.e., the time delay between $H\beta$ and the rest-frame 5100 Å continuum) with equation $\tau_{H\beta} = \tau_{\text{con-H}\beta} + (\tau_{\text{con}} - \tau_{5100})$, where τ_{con} is the rest-frame time delays between a sufficiently small wavelength (e.g., 10 Å) and the rest-frame combined $g+i$ wavelength (i.e., $(\lambda_i + \lambda_g)/2(1+z)$) which can be calculated with the method as Equation A1. We select 11 targets, and the criteria are as follows: firstly, τ_{i-g} of these targets are positive, and $S/N > 2\sigma$, where S/N is a value defined by Homayouni et al. (2019) to describe the quality of τ_{i-g} ; secondly, $\tau_{\text{con-H}\beta}$ of these targets have reliable measurements.

NGC 5548—Pei et al. (2017) measure the mean flux for 5100 Å is $f_{5100} = (7.44 \pm 0.50) \times 10^{-15} \text{ erg s}^{-1} \text{ cm}^{-2} \text{ \AA}^{-1}$ and the rest-frame $\tau_{H\beta} = 4.17 \pm 0.36$ days. The bolometric luminosity can be estimated using f_{5100} , combined with the luminosity distance $D_L = 75 \text{ Mpc}$ and the bolometric correction factor 10 (Richards et al. 2006). The black hole mass is $M_{\text{BH}} = 6.66 \times 10^7 M_{\odot}$ (Pei et al. 2017). Hence, the Eddington ratio is 0.03. Fausnaugh et al. (2016) measure multiple continuum time delays relative to 1367 Å and fit them in the same form as Eq. 1 with $\beta = 4/3$. They obtain $\tau_0 = 0.43 \pm 0.02$ days for $\lambda_0 = 1367 \text{ \AA}$. As a result, $\tau_{5100} = \tau_0(5100/1367)^{4/3} = 2.49 \pm 0.12$ days.

Mrk 817—Kara et al. (2021) measure the rest-frame $\tau_{H\beta} = 23.2 \pm 1.6$ days and multiple continuum time delays relative to the rest-frame 1869 Å (Table 4 in Kara et al. 2021). We fit the rest-frame time delay and wavelength with Eq. 1 and the fitting method in Appendix C except U and u bands which have significant contamination from BLR. We obtain $\tau_0 = 0.93 \pm 0.08$ days for $\lambda_0 = 1869 \text{ \AA}$. The corresponding $\tau_{5100} = 3.5 \pm 0.3$ days. The Eddington ratio $\dot{m} = L_{\text{bol}}/L_{\text{Edd}}$ for Mrk 817 is 0.2 (Kara et al. 2021), where $L_{\text{Edd}} = 1.26 \times 10^{38} M_{\text{BH}}/M_{\odot} \text{ erg s}^{-1}$; and the black hole mass $M_{\text{BH}} = 3.85 \times 10^7 M_{\odot}$ (Bentz & Katz 2015). Thus, the bolometric luminosity for Mrk 817 is $9.70 \times 10^{44} \text{ erg s}^{-1}$.

A.6. Equivalent width and spectral type

Equivalent width (EW), which is the line-to-continuum flux ratio, is an important parameter to describe the strengths of emission lines. We calculate the EWs of $H\beta$ for NGC 4151 at different continuum fluxes. The definition for the EW is

$$\frac{\text{EW}}{[\text{\AA}]} = \frac{f_{H\beta}}{f_{5100}}, \quad (\text{A2})$$

where $f_{H\beta}$ is the integral flux for the emission line $H\beta$, and f_{5100} is the monochromatic continuum flux for 5100 Å. Data are from the four years (from 2020 to 2024) of the Lijiang 2.4-m telescope in Yunnan Observatory spectroscopic observations for NGC 4151 (Feng et al. 2024, in preparation). Figure 6 shows that the $H\beta$ EW decreases with f_{5100} , which is consistent with the Baldwin effect (Baldwin 1977).

AGNs can be classified into different spectral types according to the line flux ratio. We follow the definition and classification of spectral types in Winkler (1992), i.e., the spectral type is decided by $H\beta$ to [O III] 5007 Å line ratio $f_{H\beta}/f_{[\text{O III}]}$. For the high-flux state, $f_{H\beta}/f_{[\text{O III}]}$ is 0.28, where $f_{H\beta}$ and $f_{[\text{O III}]}$ are average emission line fluxes for the high-flux state from Feng et al. 2024 (in preparation). For the low-flux state, due to the lack of simultaneous

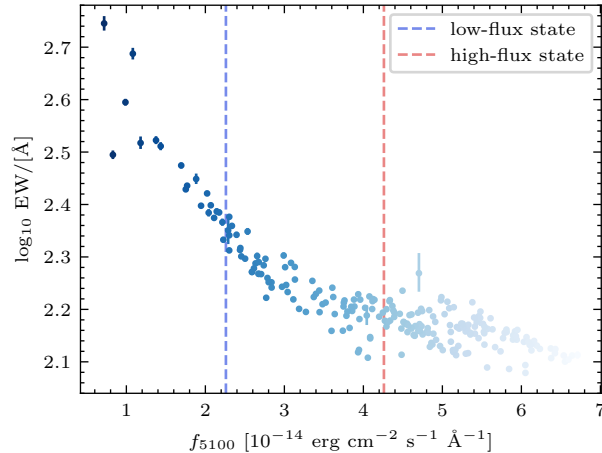


Figure 6. The evolution of equivalent width for $H\beta$ with continuum flux in NGC 4151. The x-axis is the monochromatic continuum flux for 5100 Å. The EW increases with color darkening. The vertical blue and red dashed lines represent the 5100 Å flux level of the low-flux state in E17 and the high-flux state in this work, respectively. The EW decreases with continuum flux, which implies that the effect of BLR diffuse continuum emission is smaller in the high-flux state than in the low-flux state.

spectral observations, we use the closest spectral observations during 2018–2019 monitored by the MAHA program (C23), which has a similar flux state as the low-flux state. We use the following procedures to account for the possible $H\beta$ flux offset between C23 and Feng et al. 2024 (in preparation): firstly, we use a linear function to fit the relationship between the $H\beta$ fluxes from the two works; secondly, we use the best-fitting function to convert $H\beta$ fluxes from C23 to Feng et al. 2024 (in preparation). Then, we calculate $f_{H\beta}/f_{[O III]} = 0.61$ for the low-flux state, where $f_{H\beta}$ is the average value of the calibrated C23 $H\beta$ flux, and $f_{[O III]}$ is the same as the high-flux state.

B. CONTINUUM REVERBERATION MAPPING

The time delays between observed light curves of different wavelengths can be derived using the interpolation cross-correlation function (CCF; Peterson et al. 1998), which linearly interpolates the observed light curves and calculates the correlation coefficient r between the light curves at different time delay shifts. We estimate time delays using PYCCF (Sun et al. 2018), a widely used Python code based on interpolated CCF. The time delays are calculated from the centroid of the interpolated CCF as the r -weighted delay for $r > 0.8 r_{\max}$, where r_{\max} is the maximum correlation coefficient. The time delay range for calculating the interpolated CCF is -20 days to 20 days, and the step is 0.5 days. Following the flux randomization and random subset selection procedures of Cackett et al. (2018), we perform 500 Monte Carlo iterations to establish cross-correlation centroid distributions (CCCDs). The 50%, 15.87%, and 84.13% percentiles of the CCCD are set as the measured time delay, 1σ lower and upper limits, respectively. Table 1 and Figure 2 show the measured rest-frame time delays relative to the minimum wavelength 4225 Å.

C. FITTING METHOD

We use the maximum likelihood method and the Markov Chain Monte Carlo (MCMC) chain to obtain the best-fitting relationships and parameter uncertainties. The logarithmic likelihood function is

$$\ln \mathcal{L} = -0.5 \sum [(f_n - f_{\text{model},n})^2 / \sigma_n^2 + \ln \sigma_n^2], \quad (\text{C3})$$

where f_n is the data, and $f_{\text{model},n}$ is the model value. $\sigma_n^2 = \sigma_{n,\text{err}}^2 + (\sigma_{\text{int}} f_{\text{model},n})^2$, where $\sigma_{n,\text{err}}$ is the uncertainty for f_n , and $\sigma_{\text{int}} f_{\text{model},n}$ represent the intrinsic scatter. We set uniform prior distributions for all parameters, using the MCMC code `emcee` (Foreman-Mackey et al. 2013) and the likelihood function to obtain the posterior distributions of the parameters. The best-fitting values for the parameters are the medians of the posterior distributions, 1σ uncertainties are taken as 16th–84th percentiles of the posterior distributions. The fitting method is used in the rest-frame time delay–wavelength relation fitting in Panel (b) of Figure 2 and $\log_{10}\tau_{5100}$ – $\log_{10}L_{\text{bol}}$ relation fitting in Panel (b) of Figure 3.

D. THEORETICAL MODEL

D.1. X-ray reprocessing model

The inter-wavelength time delays are explained as the light travel time differences from the X-ray corona to the disk UV/optical emission regions in the X-ray reprocessing model (e.g., Krolik et al. 1991). It is often assumed that the ratio of the external heating from the X-ray illumination to the disk internal heating at each radius is $k_X = 1/3$ (Fausnaugh et al. 2016). Note that the X-ray flux as measured by the Swift X-Ray Telescope (XRT) increases only by a factor of 1.65 from the low- to high-flux states (see Appendix A.3), similar to the variations of the optical emission. Hence, it is reasonable to assume that the mean value of k_X in the low-flux state is similar to the high-flux state. For the SSD model with X-ray reprocessing, the effective temperature profile T_{eff} is

$$T_{\text{eff}}(R) = \left(\frac{3(1+k_X)GM_{\text{BH}}\dot{M}}{8\pi\sigma R^3} \right)^{1/4}, \quad (\text{D4})$$

where G , M_{BH} , $\dot{M} = 10\dot{m}L_{\text{Edd}}/c^2$, σ and R are the Gravitational constant, black hole mass, accretion rate, the Stefan–Boltzmann constant, and the disk radius, respectively. The radiation characteristic radius $R(\lambda)$ for a given wavelength λ can be calculated based on $hc/\lambda = kT_{\text{eff}}(R(\lambda))$,

$$R(\lambda) = \left(\frac{k\lambda}{hc} \right)^{4/3} \left(\frac{3(1+k_X)GM_{\text{BH}}\dot{M}}{8\pi\sigma} \right)^{1/3}. \quad (\text{D5})$$

The time delay measured by the continuum RM is the time delay of the average radius weighted by fluxes, which is $2.49^{4/3}R(\lambda)/c$ (Fausnaugh et al. 2016). Thus, the theoretical τ_{5100} based on the SSD with X-ray reprocessing model (square dots in Figure 3) can be calculated analytically if M_{BH} and \dot{m} are specified.

Assuming that the driving light curves come from a corona located at a height $H = 5 R_S$ relative to the disk plane, where $R_S = 2GM_{\text{BH}}/c^2$ is the Schwarzschild radius. The driving light curves illuminate the disk region at radius R and azimuthal angle θ after the time delay $\tau(R, \theta)$,

$$\tau(R, \theta) = (\sqrt{R^2 + H^2} + H \cos i - R \cos \theta \sin i)/c, \quad (\text{D6})$$

where i is the disk inclination; we adopt 45° for NGC 4151 (Das et al. 2005). The long-term driving light curve is simulated with the damped random walk (DRW) model, which is a statistical model for fitting AGN light curves effectively (e.g., Kelly et al. 2009). The damping timescale, a parameter in the DRW model that describes a characteristic timescale of variability, is set as 25 days in simulations. The driving light curves heat the gas in the accretion disk with the time delay $\tau(R, \theta)$, leading to the disk temperature profile $T_{\text{eff}}(R, \theta, t)$ varying with time t . The monochromatic luminosity $L_\lambda(t)$ for a given wavelength λ at time t can be calculated by assuming perfect blackbody radiation,

$$L_\lambda(t) = \int_{R_{\text{in}}}^{R_{\text{out}}} \int_0^{2\pi} \pi B_\nu(T_{\text{eff}}(R, \theta, t)) R d\theta dR, \quad (\text{D7})$$

where $R_{\text{in}} = 3 R_S$ and $R_{\text{out}} = 10^4 R_S$ are inner and outer boundaries, respectively, $B_\nu = \frac{2h\nu^3}{c^2} \frac{1}{e^{h\nu/kT_{\text{eff}}} - 1}$ is the Planck function, and $\nu = c/\lambda$ is frequency.

Due to $\tau_{5100, \text{low}}$ being near six times the theoretical prediction for the observed X-ray or optical luminosity, we set the time delays between the corona and disk as $6\tau(R, \theta)$ in simulations, i.e., reducing the propagation velocity of X-ray emission to one-sixth of the speed of light, referred to as the “slow” X-ray reprocessing model. We simulate 100 sets of high-frequency sampling long-term light curves for both low- and high-flux states. The black hole mass and Eddington ratios are the same as observations described in Section 2. For the low-flux state, the wavelengths of mock long-term light curves are the central wavelengths in Table 1 of E17 except for X-ray bands; for the high-flux state, the wavelengths are the central wavelengths in Table 1. To improve the simulation reliability, we cut the mock long-term light curves to have the same samplings and durations as observations. In addition, we calculate the signal-to-noise $S/N = \text{Std.}(f_\lambda)/\overline{f_{\lambda, \text{err}}}$ for the observed light curves, where $\text{Std.}(f_\lambda)$ is the standard error for the light curve and $\overline{f_{\lambda, \text{err}}}$ is the mean value for the errors. We add Gaussian white noise to mock data to ensure that the mock light curves have the same S/N as observations. Next, we fit each light curve with a first-order polynomial function; this best-fitting polynomial function is subtracted from each light curve to remove the long-term trend. We calculate the time delays for the long-term trend subtracted mock light curves with the method described in Appendix B. The resulting time

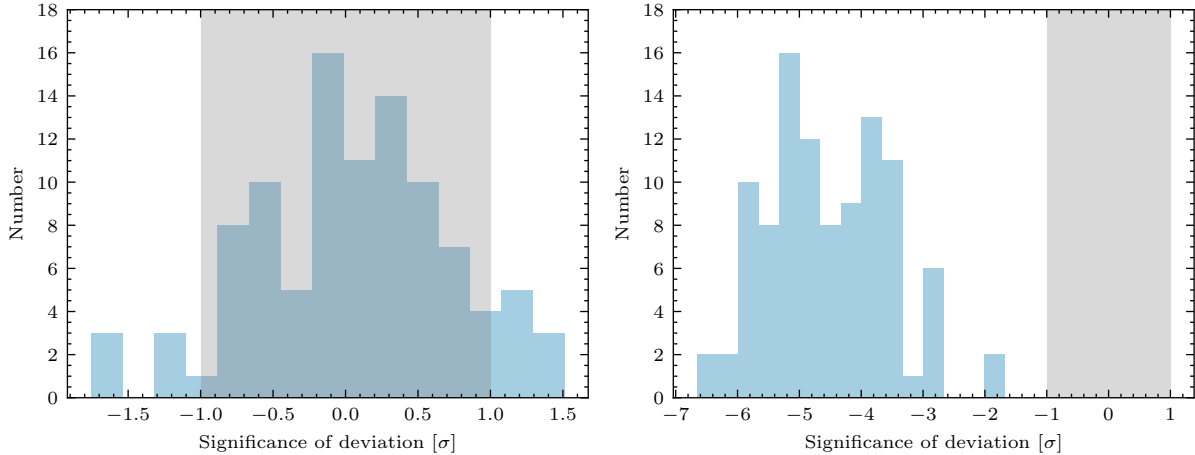


Figure 7. The significance of deviation distributions in the simulations for the “slow” X-ray reprocessing model. The left panel shows the result for the low-flux state, and the right panel shows the result for the high-flux state. The shaded area regions are 1σ confidence intervals. The “slow” X-ray reprocessing has an 83% probability of obtaining τ_0 that agrees with the low-flux state observations within 1σ uncertainty. In contrast, it is impossible to reproduce the high-flux state observation.

delays are fitted with Equation 1. The comparisons for the simulated $\tau_{0,\text{mock}}$ and observed $\tau_{0,\text{obs}}$ are shown in Figure 7. To quantitatively compare the simulated and observed results, we introduce the significance of deviation as

$$\text{S.O.D.} = \frac{\tau_{0,\text{mock}} - \tau_{0,\text{obs}}}{\sqrt{\tau_{0,\text{mock, err}}^2 + \tau_{0,\text{obs, err}}^2}}, \quad (\text{D8})$$

where $\tau_{0,\text{mock, err}}$ and $\tau_{0,\text{obs, err}}$ are 1σ uncertainties for $\tau_{0,\text{mock}}$ and $\tau_{0,\text{obs}}$, respectively. If the absolute significance of deviation is less than 1, $\tau_{0,\text{mock}}$ is statistically consistent with $\tau_{0,\text{obs}}$. The “slow” X-ray reprocessing model can reproduce the low-flux state observations but cannot account for time lags in the high-flux state.

D.2. CHAR model

The CHAR model proposes that the SMBH accretion disk is coupled magnetically with the corona. Magnetohydrodynamic (MHD) turbulence in the corona induces coherent turbulence in the accretion disk, resulting in the accretion disk having an external heating rate derived from the corona MHD turbulence. By combining the initial SSD temperature profile and the power spectral density of heating fluctuations from the corona, the accretion disk temperature fluctuation can be calculated using the thermal-energy conservation law of the SMBH accretion disk (more details in Section 2 of Sun et al. 2020). Thus, the CHAR model only requires three parameters to mock light curves: the dimensionless viscosity parameter α , M_{BH} , and \dot{m} . We adopt $\alpha = 0.3$ (King et al. 2007), M_{BH} and \dot{m} are described in Section 2. Using the CHAR model, we also mock 100 sets of high-frequency sampling long-term light curves for both low- and high-flux states. Then, we cut the long-term light curves with the same samplings and durations as observations and assign Gaussian white noise to make the mock light curves have the same S/N as observations. The significance deviation distributions for the CHAR model are shown in Figure 8. Indeed, without tweaking the model parameters, the CHAR model has 66% and 10% probabilities of reproducing $\tau_{5100,\text{low}}$ and $\tau_{5100,\text{high}}$, respectively. The main reason is that in the CHAR model, the disk magnetic disturbances caused by corona MHD turbulence respond to the disk temperature fluctuations with thermal timescales. The response thermal timescales increase with wavelengths, resulting in an additional contribution to inter-band time delays (Li et al. 2021; Chen et al. 2024). In the CHAR model (and the inhomogeneous disk model with a common large-scale temperature fluctuation; Cai et al. 2018), we find that the large continuum time delays correspond to disks with relatively large temperature fluctuations in the outer parts. Hence, the time-delay evolution in NGC 4151 suggests that the thermodynamics of the SMBH accretion disk changes substantially.

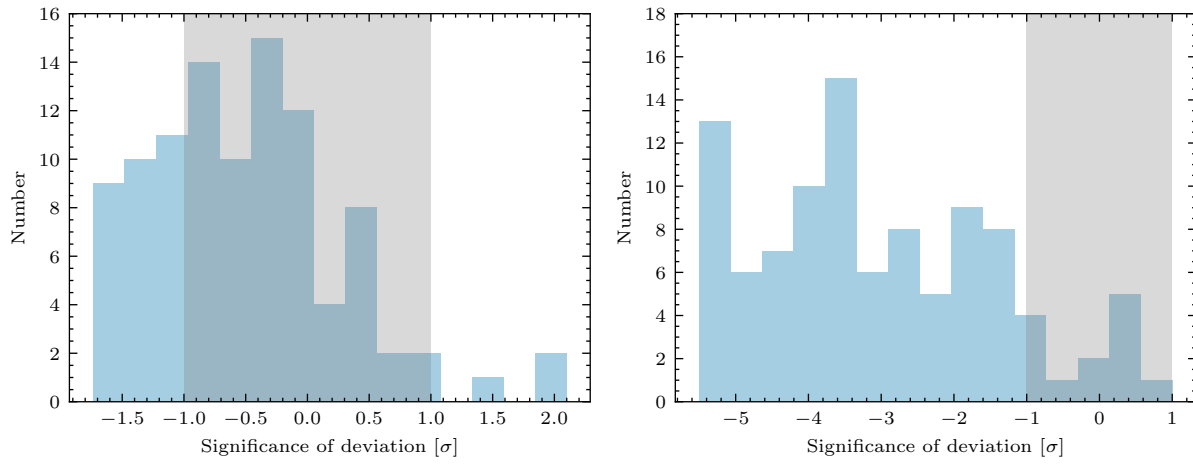


Figure 8. Same as Figure 7 but for the CHAR model. The CHAR model has a 66% probability of reproducing the low-flux state observation and a 10% probability for the high-flux state.